LETTER

doi:10.1038/nature17660

Solid-state harmonics beyond the atomic limit

Georges Ndabashimiye[1,2], Shambhu Ghimire[2], Mengxi Wu[3], Dana A. Browne[3], Kenneth J. Schafer[3], Mette B. Gaarde[3] & David A. Reis[1,2]

Strong-field laser excitation of solids can produce extremely nonlinear electronic and optical behaviour. As recently demonstrated, this includes the generation of high harmonics extending into the vacuum-ultraviolet and extreme-ultraviolet regions of the electromagnetic spectrum[1–8]. High harmonic generation is shown to occur fundamentally differently in solids and in dilute atomic gases[1–6,9–13]. How the microscopic mechanisms in the solid and the gas differ remains a topic of intense debate[1–11,14–18]. Here we report a direct comparison of high harmonic generation in the solid and gas phases of argon and krypton. Owing to the weak van der Waals interaction, rare (noble)-gas solids are a near-ideal medium in which to study the role of high density and periodicity in the generation process. We find that the high harmonic generation spectra from the rare-gas solids exhibit multiple plateaus extending well beyond the atomic limit of the corresponding gas-phase harmonics measured under similar conditions. The appearance of multiple plateaus indicates strong interband couplings involving multiple single-particle bands. We also compare the dependence of the solid and gas harmonic yield on laser ellipticity and find that they are similar, suggesting the importance of electron–hole recollision in these solids. This implies that gas-phase methods such as polarization gating for attosecond pulse generation and orbital tomography could be realized in solids.

Following the initial discovery of nonperturbative high-harmonic generation in solids[1], several experimental[2–8] and theoretical[10,11,14,15,17] investigations have aimed to understand its detailed microscopic mechanism. In particular, the roles of the high density, periodicity and bonding and how they relate to atomic high harmonic generation (HHG) remains elusive. One striking difference between the harmonics from solids and from gases is in the scaling of the high-energy cutoff. In experiments on several materials (ZnO, SiO_2 and GaSe) with pump wavelengths spanning the terahertz to the near-infrared regions of the spectrum, the cutoff was found to scale linearly with the electric field for the solid[1,4,5], whereas it scales linearly with the intensity for dilute gases[12,13]. In addition, in ZnO the ellipticity dependence was observed to be much weaker than in atomic gases[1,2,19,20]. The field-dependence of the cutoff and weak ellipticity dependence is consistent with a semi-classical Bloch oscillation model for the nonlinear intraband acceleration of electrons that have tunnelled across the direct bandgap[1,4,5,18]. The extent of the cutoff, to well beyond the maximum Bloch frequency, further suggests that the process is sensitive to details of the band structure through interactions beyond nearest neighbours[1,4]. However, interband contributions could also lead to a cutoff that is linear in the applied field, and the relative roles of inter- and intraband currents remains a topic of intense debate[1–11,14–18].

In the generalized recollision picture proposed by Vampa *et al.*[14], electrons in the conduction band recombine with their associated holes in the valence band in a manner that can be described by semi-classical trajectories. In this model, the energy of interband transitions is constrained to be less than the maximum band separation. Wu *et al.* have proposed that higher-lying conduction bands can give rise to multiple plateaus in the HHG spectrum, each with a cutoff that is limited only by the field-dressed energy spacing between bands[10]. Using a semiconductor Bloch equations treatment, Schubert *et al.* found that at far-infrared wavelengths, the HHG spectrum is dominated by intraband dynamics[5].

Until now, experiments have concentrated on covalently[1,4–8] bonded crystals. In such crystals the overlap of the atomic and molecular wavefunctions leads to a strong modification of the electronic states, making it difficult to extract material-independent aspects of the strong-field process. Rare-gas solids (RGS) are the nearest thing to a three-dimensional array of isolated atoms at high density[21], owing to the closed shell structure and high ionization potential of rare gases, and their weak bonding due to van der Waals interactions. Here we study the HHG from Ar and Kr in both gas and solid phases. We find that the HHG spectra from the solids exhibit multiple plateaus extending beyond both single-atom predictions and our measured gas harmonics for the same laser parameters. In addition, the photon energy of the solid-state harmonics greatly exceeds the maximum band separation between the highest-valence and lowest-conduction bands, suggesting the importance of solid-state effects and electronic band structure even in weakly bonded RGS.

The experiments were performed on 5-μm-thick polycrystalline Ar and Kr RGS and 3 Torr of Ar and Kr in a 1-mm-long cell for the gas (see Methods). The targets were irradiated by beams of 50 fs, 1,333 nm (0.93 eV) and 50 fs, 1,500 nm (0.82 eV) generated by a 40-fs, 1-kHz amplified Ti:sapphire laser-pumped optical parametric amplifier. The intensity of the infrared beam was calibrated using the measured spectral cutoff in the Ar and Kr gas, assuming that the cutoff energy is given by the microscopic value[12,13], $E_{cut} = I_p + 3.17U_p$, where I_p is the ionization energy and U_p is the ponderomotive energy of a free electron in the laser field.

Figure 1 shows representative high harmonic spectra from solid Ar and Kr at two intensities each, using the 1,333-nm pump (16 TW cm^{-2} and 26 TW cm^{-2} for Ar in Fig. 1a and 6.9 TW cm^{-2} and 11.4 TW cm^{-2} for Kr in Fig. 1b). The spectra from Ar and Kr are qualitatively similar, although the laser intensities for Kr are about a factor of two lower than Ar. A single plateau is evident in each at the lower intensity. For the higher intensity a second plateau is evident at ~25–33 eV for Ar and at ~19–31 eV for Kr. Figure 2a shows the harmonic spectra as a function of intensity for Ar at the 1,333-nm pump. As can be seen here, the second plateau appears suddenly over a very narrow intensity range and comprises several harmonics. The presence of the second plateau is in contrast to the experiment on HHG in dilute atomic gases, including those measured here, where only a single plateau is observed. Also shown in Fig. 2b are theoretical calculations, described below.

The high-energy extent of the second plateau notably exceeds the cutoff for the gas for the same drive wavelength and intensity. At moderate peak intensities (10 TW cm^{-2} for Kr and 20 TW cm^{-2} for Ar), the secondary plateau is almost entirely beyond the projected gas-phase cutoff. Figure 3 shows the cutoff as a function of intensity for Ar and Kr RGS and rare gases for the two different pump wavelengths.

[1]Department of Applied Physics, Stanford University, Stanford, California 94305, USA. [2]Stanford PULSE Institute, SLAC National Accelerator Laboratory, Menlo Park, California 94025, USA. [3]Department of Physics and Astronomy, Louisiana State University, Baton Rouge, Louisiana 70803, USA.

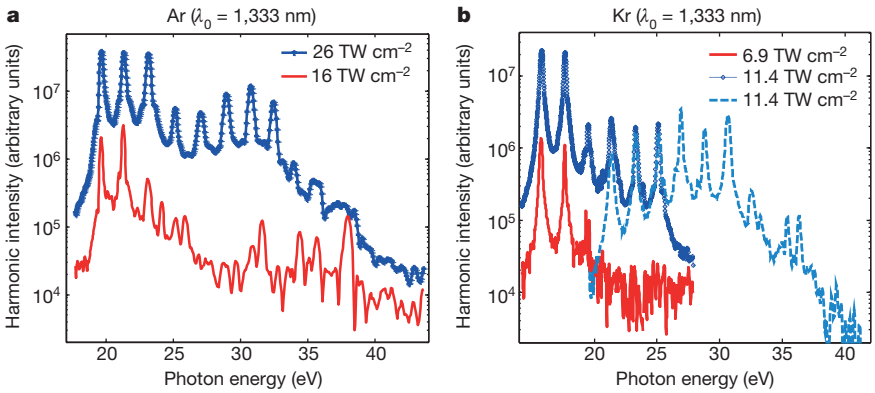

Figure 1 | Representative spectra of HHG from solid Ar and Kr on a logarithmic scale for the driving wavelength of $\lambda_0 = 1{,}333$ nm. **a**, HHG spectra from solid Ar. The spectrum taken at low intensity has only harmonics of the first plateau. At higher intensity, there are harmonics in a second plateau that start from the 27th harmonic (25 eV) and end at the 35th harmonic (32.5 eV). A third plateau is present, but its harmonics are dimmer and only its first two harmonics can be distinguished from the background. **b**, HHG spectrum from solid Kr. The spectra are taken at different spectrometer configurations and two spectra from different spectrometer configurations have been concatenated for the higher intensity. The spectra of solid Kr behave in a way similar to that of the spectrum of solid Ar except that for solid Kr the harmonics in the second plateau start at the 21st harmonic (19.5 eV) and end at the 37th harmonic (34.4 eV) and are much dimmer than in solid Ar.

The cutoff of the solid harmonics increases with increasing intensity in a nontrivial way, neither following the linear cutoff in intensity of the gas nor the square-root of intensity seen for other solids. The RGS cutoff is below the rare-gas cutoff at low intensity; however, with the sudden onset of a second plateau (as seen in Fig. 1) the RGS cutoff notably exceeds the rare-gas cutoff for the same drive wavelength and intensity. Even at moderate peak intensities (10 TW cm^{-2} for Kr and 20 TW cm^{-2} for Ar) the second plateau is almost entirely beyond the projected gas phase cutoff. The maximum photon energy detected using both wavelengths exceeds the maximum separation between the highest-valence and the lowest-conduction bands. According to Bacalis *et al.*[22], this separation is around 19 eV in solid Ar and 16 eV in solid Kr. In fact, the maximum band separation is below the higher end of the first plateau by about 3 eV in both solids.

The nontrivial scaling of the high-energy cutoff with intensity and the sudden appearance of multiple plateaus are indicative of complex solid-state behaviour. The appearance of multiple plateaus can be understood in a model in which solid-state HHG results from strong-field-driven transitions of Bloch electrons[10,11]. This behaviour is linked to the coupling of pairs of higher-lying conduction bands that are reached in a step-like process[10]. The cutoff energy and the strength of each plateau depend on the energy separation and the coupling strength between pairs of bands[23], and different plateaus can therefore exhibit different nonlinear scaling with laser intensity. Two general features of such multi-band couplings are the sudden appearance of the second plateau and the different slopes of cutoff energy versus intensity that are observed for the two plateaus.

We apply this model for HHG in solid argon by solving the time-dependent Schrödinger equation for a four-band system in which the energy levels and dipole transition elements originate from a density functional theory (DFT)-based band structure calculation[24]. In ref. 10, we show the formal equivalence between taking a Houston-state basis, where the electron and hole wavevectors k are a function of the instantaneous vector potential of the laser, and a Bloch-state basis, where the electron transitions are between different bands at fixed k. Therefore, in this single-particle picture both the interband and the intraband contribution to the HHG yield will be included when considering discrete states at $k = 0$, assuming that the tunnelling is concentrated near the direct gap at the zone centre (Γ point). Figure 2b shows the calculated harmonic spectrum as a function of laser intensity. The energies for the relevant electronic states at Γ are shown in the inset. The first plateau originates in the coupling between levels 1 and 2, and the second plateau in the coupling between 2 and 3. The dashed white curve indicates the prediction

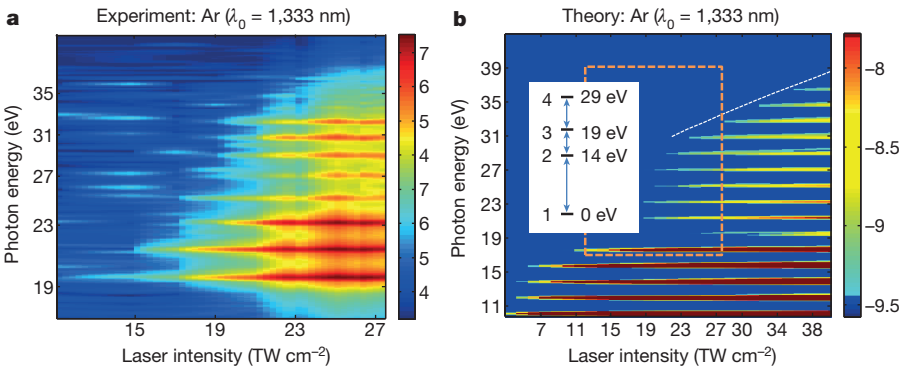

Figure 2 | Evolution of the HHG spectrum as a function of the laser intensity. The colour scale shows the logarithm of the intensity. **a**, Experimental data. HHG of solid Ar using 1,333-nm drive laser. At moderate peak intensities, the high-energy cutoff increases smoothly (up to the 27th harmonic). At around 20 TW cm^{-2} the spectral cutoff increases suddenly to the 35th harmonic. The first plateau is brighter than the second at all intensities. **b**, Theoretical results. HHG spectrum obtained by solving the time-dependent Schrödinger equation for a four-level system in which the energy separation and couplings between levels correspond to those of the Ar band-structure at the zone centre (Γ point). The calculation qualitatively and semiquantitatively reproduces the experimental data. The dashed rectangle shows the corresponding range of the experimental data. The inset shows the energy levels used in the calculations, with arrows representing the coupling between levels. The dashed white curve indicates the prediction for the cutoff energy of the second plateau based on the energy difference between field-dressed levels 1 and 3.

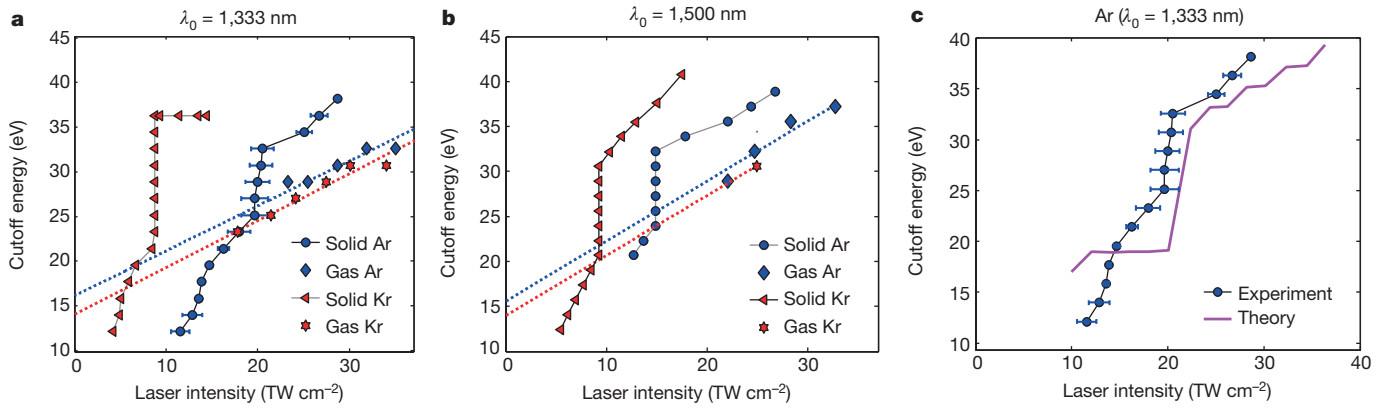

Figure 3 | Comparison of the spectral cutoff of HHG in solid and gas Ar and Kr as a function of the laser intensity. The dotted straight lines are fits of the linear cutoff of gas harmonic (blue for Ar and red for Kr). At zero laser intensity the fit was constrained to be at the ionization energies of the Ar and Kr gases ($I_p = 15.7$ eV and 14 eV), respectively. **a**, Spectral cutoff of the harmonics of 1,333 nm. For solid Ar and Kr the cutoff is not linear in the electrical field or intensity below the harmonics of photon energy 25 eV or 20 eV, respectively. In these laser intensity regions the cutoff is below that of a corresponding gas HHG (Ar and Kr). Above these photon energies, the cutoff curves abruptly turn to an almost vertical slope which indicates a switching on of new HHG processes for both solid Ar and Kr. Above 33 eV for Ar the cutoff slope decreases to a value almost equal to the slope before the sudden rise (below 25 eV). However, for solid Kr after the sudden increase in the cutoff slope, which started around 20 eV to around 35 eV, no higher harmonic was observed above 35 eV even with increasing laser intensity. The error bars are the standard deviation of repeated cutoff measurements of solid Ar HHG. **b**, Spectral cutoff of the harmonics of 1,500 nm. For both solid Ar and Kr, the HHG cutoff respectively below 25 eV and 20 eV is almost linear in intensity and this cutoff is below of that of the corresponding gases. Above these photon energies the slope of the cutoff curves becomes vertical, as for the 1,333-nm case. However, for solid Kr the sudden increase in the cutoff energy ends at 31 eV, and a less steep cutoff develops between 31 eV and 41 eV. **c**, Comparison of measured cutoff and calculated cutoff. There is qualitative agreement between the measurement and the calculation. The error bars are the standard deviation of repeated cutoff measurements of solid Ar HHG.

for the cutoff energy of the second plateau based on the energy difference between the field-dressed levels 1 and 3 (see Methods). The calculated values of the first and second cutoff energies compare reasonably well to those of the experiment, as shown in Fig. 2b and Fig. 3c. We note that to get the best agreement on the location and scaling of the plateaus to the experimental results, we have adjusted the dipole coupling strengths obtained from DFT (see Methods). In this case, the coupling strengths between levels 1 and 2, between levels 2 and 3, and between levels 3 and 4 are comparable. This is indicative of a periodic system in which electrons are strongly localized around the individual atomic sites rather than the more delocalized electron behaviour one would find in covalently bonded semiconductors such as ZnO.

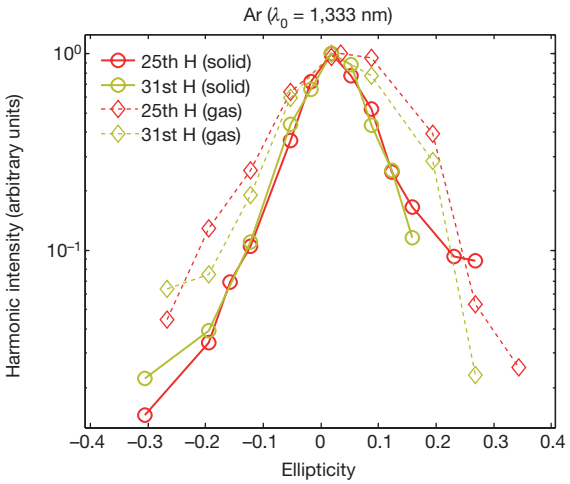

Figure 4 | Comparison of ellipticity dependence of the 25th and 31st harmonics from solid and gas-phase Ar at similar peak fields. The 25th and 31st harmonics lay in the first and second plateaus, respectively, for solid Ar. The harmonic intensity shows a similar ellipticity dependence for the two orders from both the solid and gas. The sensitivity to ellipticity is at least as strong in the solid as in the gas.

This conclusion is supported by the measured strong ellipticity dependence in RGS compared to what was previously measured in ZnO[1]. In Fig. 4, we show our measurements of the ellipticity dependence for two representative harmonics of gas and solid Ar. These harmonics were chosen such that they fall within the ranges of the first and second plateaus for the RGS (25th and 31st harmonics, respectively). These harmonics show similar ellipticity dependence for the different orders. Moreover, the solid-state harmonics are at least as sensitive to ellipticity as is the gas. We note that the strong ellipticity dependence in atomic and molecular HHG has been attributed to the transverse momentum of the tunnel-ionized electron causing the returning electron wavepacket to miss the parent ion[19,20]. That characteristic has been used in the generation of isolated attosecond pulses[25] and in imaging of molecular orbitals[26]. Our observation of strong ellipticity dependence of harmonics in RGS opens up similar opportunities for attosecond pulse generation and imaging of electronic wavefunctions in the solid state.

We have measured high harmonics from solid and gas-phase Ar and Kr. The solid-state harmonics include multiple plateaus whose high-energy cutoff extends beyond the atomic limit. This demonstrates the importance of solid-state effects even in the weakly bound van der Waals solids. We show that the multiple plateaus can be accommodated in a single-particle picture, similar to the single-active electron models used to calculate gas-phase harmonics in both atomic and molecular systems, in which only one electron is assumed to interact with the laser field[12,13]. We further note that the appearance of the second plateau occurs at very nearly twice the exciton energy (~24 eV in Ar and ~20 eV in Kr). Although this could be indicative of many body-effects beyond the single-particle picture, such a model is not required to capture the general features seen in the experiment. In either case, the important difference between the solid and the gas is that the solid involves transitions between bound states created by band folding due to the periodic potential. In this sense there is no free-particle continuum for electrons in the solid, or equivalently, even in the case of RGS, the effect of the periodic potential cannot be neglected.

Online Content Methods, along with any additional Extended Data display items and Source Data, are available in the online version of the paper; references unique to these sections appear only in the online paper.

Received 11 December 2015; accepted 4 March 2016.
Published online 6 June 2016.

1. Ghimire, S. *et al.* Observation of high-order harmonic generation in a bulk crystal. *Nature Phys.* **7,** 138–141 (2011).
2. Ghimire, S. *et al.* Strong-field and attosecond physics in solids. *J. Phys. At. Mol. Opt. Phys.* **47,** 204030 (2014).
3. Ghimire, S. *et al.* Redshift in the optical absorption of ZnO single crystals in the presence of an intense midinfrared laser field. *Phys. Rev. Lett.* **107,** 167407 (2011).
4. Luu, T. T. *et al.* Extreme ultraviolet high-harmonic spectroscopy of solids. *Nature* **521,** 498–502 (2015).
5. Schubert, O. *et al.* Sub-cycle control of terahertz high-harmonic generation by dynamical Bloch oscillations. *Nature Photon.* **8,** 119–123 (2014).
6. Hohenleutner, M. *et al.* Real-time observation of interfering crystal electrons in high-harmonic generation. *Nature* **523,** 572–575 (2015).
7. Vampa, G. *et al.* Linking high harmonics from gases and solids. *Nature* **522,** 462–464 (2015).
8. Vampa, G. *et al.* All-optical reconstruction of crystal band structure. *Phys. Rev. Lett.* **115,** 193603 (2015).
9. Ghimire, S. *et al.* Generation and propagation of high-order harmonics in crystals. *Phys. Rev. A* **85,** 043836 (2012).
10. Wu, M., Ghimire, S., Reis, D. A., Schafer, K. J. & Gaarde, M. B. High-harmonic generation from Bloch electrons in solids. *Phys. Rev. A* **91,** 043839 (2015).
11. Korbman, M., Yu Kruchinin, S. & Yakovlev, V. S. Quantum beats in the polarization response of a dielectric to intense few-cycle laser pulses. *New J. Phys.* **15,** 013006 (2013).
12. Corkum, P. B. Plasma perspective on strong field multiphoton ionization. *Phys. Rev. Lett.* **71,** 1994–1997 (1993).
13. Krause, J. L., Schafer, K. J. & Kulander, K. C. High-order harmonic generation from atoms and ions in the high intensity regime. *Phys. Rev. Lett.* **68,** 3535–3538 (1992).
14. Vampa, G. *et al.* Theoretical analysis of high-harmonic generation in solids. *Phys. Rev. Lett.* **113,** 073901 (2014).
15. McDonald, C. R., Vampa, G., Corkum, P. B. & Brabec, T. Interband Bloch oscillation mechanism for high-harmonic generation in semiconductor crystals. *Phys. Rev. A* **92,** 033845 (2015).
16. Vampa, G., McDonald, C. R., Orlando, G., Corkum, P. B. & Brabec, T. Semiclassical analysis of high harmonic generation in bulk crystals. *Phys. Rev. B* **91,** 064302 (2015).
17. Higuchi, T., Stockman, M. I. & Hommelhoff, P. Strong-Field Perspective on High-Harmonic Radiation from Bulk Solids. *Phys. Rev. Lett.* **113,** 213901 (2014).
18. Golde, D., Meier, T. & Koch, S. W. Microscopic analysis of high-harmonic generation in semiconductor nanostructures. *Phys. Status Solidi C* **6,** 420–423 (2009).
19. Budil, K. S., Salières, P., L'Huillier, A., Ditmire, T. & Perry, M. D. Influence of ellipticity on harmonic generation. *Phys. Rev. A* **48,** R3437–R3440 (1993).
20. Burnett, N. H., Kan, C. & Corkum, P. B. Ellipticity and polarization effects in harmonic generation in ionizing neon. *Phys. Rev. A* **51,** R3418–R3421 (1995).
21. Klein, M. L. & Venables, J. A. *Rare Gas Solids* 123 (Academic Press, 1976).
22. Bacalis, N. C., Papaconstantopoulos, D. A. & Pickett, W. E. Systematic calculations of the band structures of the rare-gas crystals neon, argon, krypton, and xenon. *Phys. Rev. B* **38,** 6218–6226 (1988).
23. Gauthey, F. I., Garraway, B. M. & Knight, P. L. High harmonic generation and periodic level crossings. *Phys. Rev. A* **56,** 3093–3096 (1997).
24. Blaha, P., Schwarz, K., Madsen, G., Kvasnicka, D. & Luitz, J. *WIEN2k, An Augmented Plane Wave Plus+Local Orbitals Program for Calculating Crystal Properties* (TU Wien, 2001).
25. Shan, B., Ghimire, S. & Chang, Z. Generation of the attosecond extreme ultraviolet supercontinuum by a polarization gating. *J. Mod. Opt.* **52,** 277–283 (2005).
26. Itatani, J. *et al.* Tomographic imaging of molecular orbitals. *Nature* **432,** 867–871 (2004).

Acknowledgements At Stanford/SLAC, this work was supported by the US Department of Energy, Office of Science, Office of Basic Energy Sciences, through the AMOS programme within the Chemical Sciences Division (G.N., D.A.R.) and the Office of Science Early Career Research Program (S.G.). At Louisiana State University this work is supported by the National Science Foundation under grant number PHY-1403236. Solid Ar samples were characterized at Stanford Synchrotron Radiation Lightsource, SLAC National Accelerator Laboratory, the use of which is supported by the US Department of Energy, Office of Science, Office of Basic Energy Sciences under contract number DE AC02-76SF00515.

Author Contributions G.N., S.G. and D.A.R. conceived the experiments. G.N. performed the experiment and analysed the data. M.W., K.J.S., and M.B.G. developed the single electron laser excitation theory and performed the calculation. D.A.B. performed the DFT calculations. All authors contributed to the interpretation of the results and writing of the manuscript.

Author Information Reprints and permissions information is available at www.nature.com/reprints. The authors declare no competing financial interests. Readers are welcome to comment on the online version of the paper. Correspondence and requests for materials should be addressed to D.A.R. (dreis@stanford.edu) or G.N. (ndabashi@stanford.edu).

METHODS

Experiments. The RGS samples were grown inside an ultrahigh vacuum ($<10^{-7}$ mbar) chamber at a temperature of 20 K for Ar and 27 K for Kr. A closed-circuit cryostat was used to cool down a silicon wafer with 30-nm-thick silicon nitride windows (0.5 mm × 0.5 mm). The silicon nitride was used as the substrate for growing the crystals. The Ar and Kr crystals were grown at a rate of about 1 μm min^{-1} and the thickness was measured using thin-film interference of a HeNe laser beam. Growth occurred in the absence of the strong-field infrared pump beam. The silicon nitride windows were ablated at the focal spot by the strong-field pump subsequent to growth, leaving a free-standing RGS film. Sublimation of the samples was found to be negligible over the course of the exposure by the laser when excited below the damage threshold. The damage threshold was determined to be ∼30 TW cm^{-2} for solid Ar and ∼15 TW cm^{-2} for solid Kr by both visual inspection and loss of the harmonic emission and for the conditions reported here. The harmonic spectra were measured using a home-built spectrometer consisting of a flat-field imaging grating (Hitachi 001-0639) and micro channel plate (MCP) detection system. The MCP was mounted on movable bellows which permitted us to observe different spectral regions between 10 eV and 45 eV. The high energy cutoff was determined by the intensity at which the highest harmonic is approximately three times the noise on the MCP, ignoring peaks that are inconsistent across multiple measurements. We note that the intensities used here are about an order of magnitude lower than in the typical gas-phase HHG experiments, and therefore reaching the fully phase-matched conditions in the gas would require a much higher pressure than we can achieve with our experimental setup. Because of that technical limitation, we performed measurements at relatively high peak intensity (>20 TW cm^{-2} in Ar gas), and extrapolated the high-energy cutoff scaling results to the moderate peak intensity scales. The intercept on the cutoff energy axis corresponds to the ionization energy threshold, as expected. For the ellipticity dependence measurements, the polarization was varied using a quarter-wave plate. The peak field along the major axis was kept constant by adjusting the pulse energy.

The Ar films were characterized under the same growth conditions by X-ray diffraction at the Stanford Synchrotron Radiation Lightsource and the size of the crystal grains was found to be at least 100 nm. The sample thickness was chosen empirically to be thick enough to provide mechanical stability against the strong-field excitation and substrate ablation, but thin enough to mitigate propagation effects, including cascaded nonlinear wavemixing, which we observed to depend on film thickness[27]. The focal spot upon propagation through the solid film and divergence of the harmonics were measured to be independent of incident intensity, falling within 10% of their nominal values.

Calculations. The argon band structure and dipole transition elements are calculated using DFT. The DFT calculations employ the linear augmented plane-wave method implemented in Wien2k[24]. The calculations use a muffin-tin radius of 3.0 Bohr, a k-point grid of 33 × 33 × 33 in the Brillouin zone, and a plane-wave energy cutoff of 50 atomic units. The DFT code uses the Perdew–Burke–Ernzeroff generalized gradient approximation (GGA) functional[28]. Since DFT produces an energy gap that is too small, a modified Becke–Johnson correction[29] is applied to the conduction-bands energies to obtain better agreement with the experimental band structure.

We next use the band structure and the transition matrix elements to solve the time-dependent Schrödinger equation (TDSE) in k-space, in which different k-values are decoupled. The harmonic spectrum is obtained as the Fourier transform of the time-dependent current calculated from the TDSE solution[10]. Our initial condition is a delocalized Bloch wavefunction (only $k=0$) located at the highest symmetric point, Γ, on the valence band. For simplicity we include only the four lowest strongly coupled bands, meaning that we are solving the TDSE for a four-level system, in the Bloch basis[10]. We have established that including additional higher bands makes only a negligible change to the harmonic spectrum, whereas excluding any of the four lowest bands makes a large difference. We adjust the dipole transition matrix elements so that the couplings between levels 1 and 2, between levels 2 and 3, and between levels 3 and 4 are roughly equal (in atomic units the couplings are $\mu_{1,2}=0.62$, $\mu_{2,3}=0.41$, and $\mu_{3,4}=-0.61$) and ignore all other couplings. We justify this adjustment on the grounds that the experiment averages over all orientations, and precise dipole-matrix elements for higher bands are difficult to extract from DFT. The four strongly coupled levels in our model represent the simplest possible description of the coupling between clusters of bands, which would be expected to occur in steps, with approximately equal coupling strengths.

In the four-level picture, the multiple plateaus simply come from transitions between the instantaneous, field-dressed, eigenstates of the system. For a four-level system driven by a laser field $F(t)$, the Hamiltonian can be written as

$$H=\begin{pmatrix} \omega_1 & \mu_{12}F(t) & 0 & 0 \\ \mu_{12}F(t) & \omega_2 & \mu_{23}F(t) & 0 \\ 0 & \mu_{23}F(t) & \omega_3 & \mu_{34}F(t) \\ 0 & 0 & \mu_{34}F(t) & \omega_4 \end{pmatrix}$$

where ω_i is the energy of the band i and μ_{ij} is the dipole transition between levels i and j. The energies of the instantaneous eigenstates E_i can be calculated by diagonalizing the Hamiltonian. Then the cutoff energy for the first plateau will be given by the maximum energy difference between the field-dressed levels, $(E_2-E_1)_{\max}$, which scales approximately linearly with the laser field strength[10]. Likewise the cutoff energy for the second plateau will be $(E_3-E_1)_{\max}$. This prediction agrees very well with the two harmonic cutoffs visible in Fig. 2b.

27. Ndabashimiye, G., Ghimire, S., Reis, D. & Nicholson, D. Measurement of coherence lengths of below threshold harmonics in solid argon. *Opt. Soc. Am. Tech. Dig.* QW1A.7 http://dx.doi.org/10.1364/CLEO_QELS.2013.QW1A.7 (2013).
28. Perdew, J. P., Burke, K. & Ernzerhof, M. Generalized gradient approximation made simple. *Phys. Rev. Lett.* **77,** 3865–3868 (1996).
29. Tran, F. & Blaha, P. Accurate band gaps of semiconductors and insulators with a semilocal exchange-correlation potential. *Phys. Rev. Lett.* **102,** 226401 (2009).